APL Photonics

Spatial and spectral mode-selection effects in topological lasers with frequency-dependent gain

Cite as: APL Photonics **6**, 050803 (2021); https://doi.org/10.1063/5.0041124
Submitted: 19 December 2020 . Accepted: 08 April 2021 . Published Online: 03 May 2021

Matteo Seclì, Tomoki Ozawa, Massimo Capone, and Iacopo Carusotto

Spatial and spectral mode-selection effects in topological lasers with frequency-dependent gain

Cite as: APL Photon. 6, 050803 (2021); doi: 10.1063/5.0041124
Submitted: 19 December 2020 • Accepted: 8 April 2021 •
Published Online: 3 May 2021

Matteo Seclì,[1,a] Tomoki Ozawa,[2] Massimo Capone,[1,3] and Iacopo Carusotto[4]

AFFILIATIONS

[1] International School for Advanced Studies (SISSA), Via Bonomea 265, I-34136 Trieste, Italy
[2] Advanced Institute for Materials Research, Tohoku University, Sendai 980-8577, Japan
[3] CNR-IOM Democritos, Via Bonomea 265, I-34136 Trieste, Italy
[4] INO-CNR BEC Center and Dipartimento di Fisica, Università di Trento, I-38123 Povo, Italy

Note: This paper is part of the APL Photonics Special Topic on Synthetic Gauge Field Photonics.
[a] **Author to whom correspondence should be addressed:** matteo.secli@sissa.it

ABSTRACT

We develop a semiclassical theory of laser oscillation into a chiral edge state of a topological photonic system endowed with a frequency-dependent gain. As an archetypal model of this physics, we consider a Harper–Hofstadter lattice embedding population-inverted, two-level atoms as a gain material. We show that a suitable design of the spatial distribution of gain and its spectral shape provides flexible mode-selection mechanisms that can stabilize single-mode lasing into an edge state. Implications of our results for recent experiments are outlined.

I. INTRODUCTION

Topological lasers (in short, *topolasers*) are one of the most promising applications of topological photonics. Such devices are obtained by including a suitable gain material in a topological system so as to induce laser oscillation in a topological edge state.[1,2] Stimulated by pioneering theoretical proposals,[3–7] experimental realizations were first reported for the zero-dimensional edge states of one-dimensional arrays.[8–12] Extension to nanolasers based on zero-dimensional corner states of two-dimensional lattices was reported in Refs. 13 and 14.

Scaling up in dimension, the crucial advantages for optoelectronic applications offered by topological lasing into the one-dimensional edge modes of a two-dimensional lattice have been theoretically highlighted:[3–5,15,16] the topological protection of chirally propagating one-dimensional edge modes appears as a promising strategy toward an efficient phase-locking of the laser oscillation at the different sites. In this way, gain can be distributed over a large number of sites while maintaining a globally stable single-mode coherent emission, which is very promising to realize high-power coherent sources. Experiments along these lines were reported shortly afterward using photonic crystals under a strong magnetic field[17] and arrays of coupled ring microcavities,[18] followed by more recent valley-Hall quantum cascade[19] and telecom-wavelength[20] lasers.

These experimental advances have stimulated an active theoretical research to characterize the peculiar properties of the novel devices.[16,21–23] Whereas the experiments in Refs. 17 and 18 have shown a clean single-mode emission from topolasers, the possibility of secondary instabilities as a result of the interplay of optical nonlinearities and slow carrier dynamics has been theoretically pointed out in Ref. 21. A semiclassical study of the novel features introduced by the chirality of the lasing state was reported in Refs. 23 and 24. Extensive theoretical studies based on a stochastic approach have anticipated the robustness of the long-time coherence against static disorder by including quantum and thermal fluctuations into an idealized model of topolaser.[16] Finally, the specific features of the weaker topologically protected but experimentally much less demanding topological lasing in valley Hall systems have been theoretically discussed in Refs. 25 and 26.

In this work, we investigate the various mode-selection mechanisms that determine whether a topolaser device is going to lase in an edge state or in a bulk state. Rather than dealing with the complex nonlinear dynamics of the lasing state,[16,21,23] we focus our attention on identifying the mode that is responsible for the first instability of the vacuum state. This is a common strategy in laser physics[27] and typically provides a good intuition on the system behavior not too far above threshold. For instance, if different modes of the laser resonator have different spatial profiles, a specific mode can be selected just by increasing its spatial overlap with the gain material. In the context of topolasing, a suitable spatial distribution of gain/losses was exploited in Ref. 12 to favor laser operation in a protected zero mode of a one-dimensional lattice. Theoretical investigations on the impact of nonlinearities on such spatial mode-selection mechanisms and on possible transition to complex regimes with time-dependent power oscillations were reported in Ref. 22.

Here, we go beyond these works by including the additional spectral mode-selection mechanism coming from the frequency dependence of gain. In its simplest formulation, spectral mode-selection allows us to suppress competing cavity modes that are well separated in frequency by tuning a narrowband gain material in the spectral vicinity of the desired mode. In particular, we take motivation from the recent topolaser experiment in Ref. 17 to investigate how a subtle combination of spectral and spatial mode-selection mechanisms can conspire to stabilize laser oscillation into a chiral edge state. As an important outcome of our analysis, we point out a possible mechanism for the still unexplained experimental observation[17] of single-mode emission under a homogeneous pump with no need of concentrating pumping along the edge as it was instead done in other topolaser realizations, e.g., in Ref. 18.

From a conceptual perspective, topological lasing under spatially homogeneous pumps is of special interest as it allows for a direct connection to the general concepts of non-Hermitian topology:[2,28,29] in such a geometry, each region maintains, in fact, its (discrete) translational invariance. Bulk bands can thus be classified in terms of suitably generalized non-Hermitian topological invariants including the effect of gain and losses within the unit cell, and the value of the topological invariants can be then connected to the presence and the properties of edge states at the boundaries.

The structure of this article is the following. In Sec. II, we introduce the physical system under investigation, namely, a photonic Harper–Hofstadter lattice embedding population-inverted two-level atoms (TLAs) as gain medium, and we develop the theoretical model based on a Bloch–Harper–Hofstadter set of equations. In Sec. III, we show how the use of a narrowband gain stabilizes the edge mode lasing even when the gain material is uniformly distributed across the whole system. In Sec. IV, we show how a suitable combination of spectral and spatial selection mechanisms is able to stabilize the edge mode lasing under weak conditions on the gain lineshape and its spatial localization. The experimental implications of our results are discussed in Sec. V. Conclusions are finally drawn in Sec. VI. Additional details on the derivation of the theoretical models, the topological lasing features, and our spatial-spectral mode-selection mechanism are given in the supplementary material.

II. THE THEORETICAL FRAMEWORK

In this section, we summarize the theoretical model used for our calculations. As an archetypal model, we consider a photonic Harper–Hofstadter lattice where optical gain is introduced by including population-inverted two-level atoms at each site. For a complete derivation of the equations of this *Bloch–Harper–Hofstadter* model, we refer the interested reader to Sec. S.1 of the supplementary material.

Harper–Hofstadter lattices were realized in integrated photonic devices by engineering the hopping links between neighboring microring resonators[30] and, in this form, were used in the topolaser experiment of Ref. 18. Even though our study makes use of the Harper–Hofstadter model as a paradigmatic example of the topological lattice, our conclusions extend to a wide variety of discrete or continuous topological photonics systems[1] and, in particular, help shining light on the photonic crystal experiment of Ref. 17.

In the recent experimental implementations, gain is obtained by inserting optically pumped quantum wells[17,18] or electrically driven quantum cascade heterostructures[19] into a solid-state topological lattice. Here, we will not dwell into the complexities of the microscopic physics of specific gain materials, but we will base our discussion on a simplest description in terms of population-inverted two-level atoms. Despite its simplicity, this approach provides a reasonably accurate effective description of a wide range of actual media and, in particular, is able to correctly include the frequency dependence of gain, which is the focus of our analysis.

A. The Bloch–Harper–Hofstadter model

We consider a two-dimensional Harper–Hofstadter lattice[1,31] where neighboring sites are connected through a hopping Hamiltonian with a non-trivial hopping phase. In the Landau gauge, this can be written as

$$H_{\mathrm{bare}} = \hbar\omega_{\mathrm{cav}}\sum_{m,n} a^{\dagger}_{m,n}a_{m,n} - J\sum_{m,n}\left\{a^{\dagger}_{m,n}a_{m+1,n} + e^{-i2\pi\vartheta m}a^{\dagger}_{m,n}a_{m,n+1} + \mathrm{h.c.}\right\}, \tag{1}$$

where $a^{\dagger}_{m,n}$ ($a_{m,n}$) is the operator that creates (annihilates) a photon at the (m,n) site. All sites are assumed to have a bare photon frequency ω_{cav}, the real and positive parameter J quantifies the hopping strength, and $\vartheta = 1/4$ is the flux per plaquette of the synthetic gauge field that is responsible for the topological properties.

The topological features are easily understood by considering a strip geometry with periodic boundary conditions along one direction (y) and open boundary conditions along the other (x). As shown in the right panel of Fig. 1, the energy dispersion in the first Brillouin zone $k_y \in [-\pi,\pi]$ shows four bulk bands: the central two bands touch at Dirac points, while the two external ones are separated by finite bandgaps, symmetrically located at positive and negative energies. The Chern numbers of the bands are, from bottom to top, $\mathcal{C} = -1, +2, -1$, where the two central bands have been considered as a single band in the calculation of the Chern number because of the degeneracy in the Dirac points. In agreement with these Chern numbers, each bandgap hosts one chiral edge mode and the edge modes in each topological gap have opposite chiralities, the one in the negative (positive) energy gap propagating in the

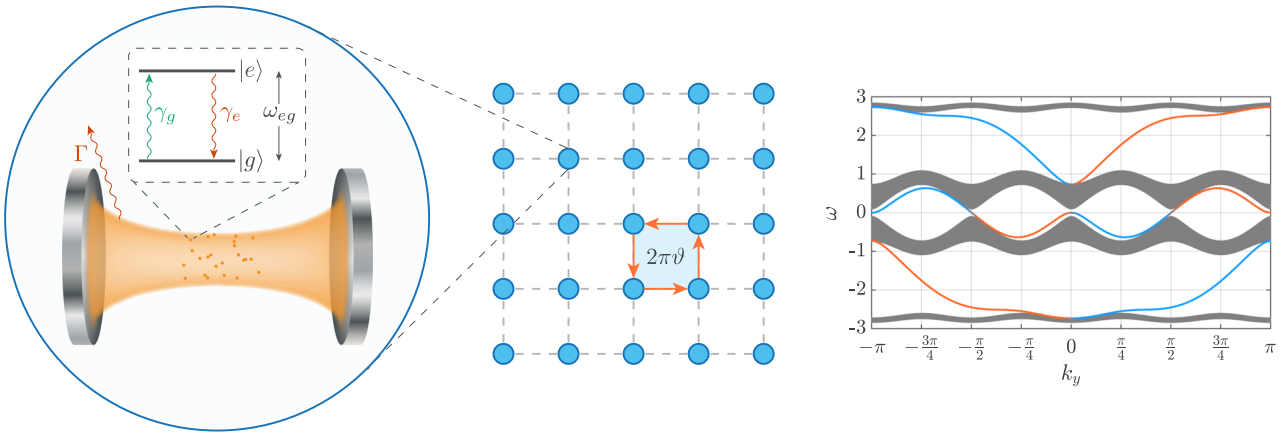

FIG. 1. Left and central panels: scheme of a Harper–Hofstadter lattice consisting of an array of photonic cavities embedding two-level atoms (TLAs). The energy difference between the two atomic levels is ω_{eg}; pumping of the atoms from $|g\rangle$ to $|e\rangle$ occurs at a rate γ_g, while their spontaneous decay from $|e\rangle$ to $|g\rangle$ occurs at a rate γ_e. All cavities decay at an equal loss rate Γ. The synthetic magnetic field is included as a non-trivial hopping phase: a photon that hops around a plaquette (orange arrows) picks up an extra phase $2\pi\vartheta$ due the synthetic magnetic flux, in our case $\vartheta = 1/4$. Right panel: plot of the energy dispersion for a $\vartheta = 1/4$ Harper–Hofstadter lattice with periodic boundary conditions along y and $N_x = 39$ sites with open boundary conditions along x. The gray bands correspond to bulk states. The colorful lines indicate the topologically protected edge states, with red (blue) color indicating localization on the right (left) edge.

counter-clockwise (clockwise) direction. For the strip geometry considered in this plot, two edge modes are present in each gap, unidirectionally propagating in opposite directions along y. Their topological protection from disorder stems from their spatial localization on opposite $x = 1, N_x$ edges of the lattice, which suppresses back-scattering.

As sketched in Fig. 1, each site is modeled as a photonic resonator of frequency $\omega_{\rm cav}$ and decay rate Γ in which a photon is created (annihilated) by $a^\dagger$ (a). Each resonator is provided with a frequency-dependent gain medium, which is modeled here as a collection of N population-inverted two-level atoms (TLAs). At each site, the dynamics of the atoms forming the gain medium is then described by the following Hamiltonian:

$$H_{{\rm at},N} = \sum_{j=1}^{N} H_{{\rm at},1}^{(j)} = \sum_{j=1}^{N} \left\{ \frac{1}{2}\hbar\omega_{eg}\sigma_j^z + \hbar g\left(\sigma_j^+ a + a^\dagger \sigma_j^-\right)\right\}, \tag{2}$$

where $\omega_{eg} = \omega_e - \omega_g$ is the energy difference between the atomic levels, the light–atom coupling g is assumed to be equal for all $j = 1, \ldots, N$ atoms and, for each atom, $\sigma^+ = |e\rangle\langle g|$ and $\sigma^- = (\sigma^+)^\dagger = |g\rangle\langle e|$ are the raising and lowering operators between the ground $|g\rangle$ and excited $|e\rangle$ states. Analogously, the atomic population difference on each atom is quantified by the $\sigma^z = |e\rangle\langle e| - |g\rangle\langle g|$ operator. Each TLA is incoherently pumped from the ground to the excited state at a pumping rate γ_g, while the reverse spontaneous decay from $|e\rangle$ to $|g\rangle$ occurs at a rate γ_e.

Under a mean-field approximation, we replace the photon field operators $a_{m,n}$ with their classical C-number expectation values $\alpha_{m,n} = \langle a_{m,n}\rangle$ and we assume the atomic density matrix to have a factorized form. The one-atom Hamiltonian terms $H_{{\rm at},1}^{(j)} \equiv H_{{\rm at},1}$ and the one-atom density matrices $\rho_{\rm at}$ are then equal for all atoms at a given site, and their dynamics is captured by a Lindblad master equation of the form

$$\frac{d\rho_{\rm at}}{dt} = -\frac{i}{\hbar}[H_{{\rm at},1}, \rho_{\rm at}] + \sum_{s=e,g}\gamma_s\left(L_s\rho_{\rm at}L_s^\dagger - \frac{1}{2}\left\{L_s^\dagger L_s, \rho_{\rm at}\right\}\right), \tag{3}$$

where the first term gives the coherent evolution induced by the atom-field dynamics in (2) and $L_e = |g\rangle\langle e| = \sigma^-$ and $L_g = |e\rangle\langle g| = \sigma^+$ are the jump operators for the decay and pumping processes.

Projecting (2) and (3) onto the atomic ground and excited states then recovers the Bloch equations of the semiclassical theory of lasers.[32,33] Together with the field dynamics determined by the hopping Hamiltonian (1), these equations constitute the full set of equations of our Bloch–Harper–Hofstadter model. Measuring all energies and times in units of J and J^{-1}, respectively, and setting the frequency zero at the empty cavity frequency $\omega_{\rm cav}$, these equations have the form

$$\begin{cases} \dot\rho_{ee}^{m,n} = \gamma_g\rho_{gg}^{m,n} - \gamma_e\rho_{ee}^{m,n} + i\left(\alpha_{m,n}\rho_{ge}^{m,n} - \alpha_{m,n}^*\rho_{eg}^{m,n}\right), \\ \dot\rho_{gg}^{m,n} = \gamma_e\rho_{ee}^{m,n} - \gamma_g\rho_{gg}^{m,n} - i\left(\alpha_{m,n}\rho_{ge}^{m,n} - \alpha_{m,n}^*\rho_{eg}^{m,n}\right), \\ \dot\rho_{eg}^{m,n} = -i(\omega_{eg} - i\gamma)\rho_{eg}^{m,n} - i\alpha_{m,n}\left(\rho_{ee}^{m,n} - \rho_{gg}^{m,n}\right), \\ \dot\alpha_{m,n} = -\Gamma\alpha_{m,n} + iG\rho_{eg}^{m,n} + i(\alpha_{m+1,n} + \alpha_{m-1,n} \\ \qquad + e^{-i2\pi\vartheta m}\alpha_{m,n+1} + e^{+i2\pi\vartheta m}\alpha_{m,n-1}), \end{cases} \tag{4}$$

where $\rho_{ee}^{m,n}$ ($\rho_{gg}^{m,n} = 1 - \rho_{ee}^{m,n}$) is the average atomic population of the excited (ground) state of the atoms located at site (m, n) and $\rho_{eg}^{m,n}$ is the corresponding coherence. In the following, we will assume, for simplicity, that no additional decay channel acts on the atomic coherence ρ_{eg} in addition to the unavoidable ones coming from pumping and decay, $\gamma = \gamma_{eg} = (\gamma_g + \gamma_e)/2$.

The efficiency of the gain process enters via the $G \doteq g^2N$ coupling strength, proportional to the number of atoms N per site and to the square of the elementary light–atom coupling g. Indicating

with V the effective field volume at each site, the light–atom coupling scales as usual as $V^{-1/2}$ (see Sec. S.1 of the supplementary material), which makes G proportional to the atomic density N/V. If a real atomic gas is used as the gain material, the gain strength can be tuned by changing the density of the gas. In a solid state photonic crystal where the TLAs are used to model a more complex electronic dynamics in the material, the same effect can be achieved by varying the filling factor within the unit cell and/or the overlap of the Bloch mode with the gain material. To keep our analysis as simple as possible, in the following we will use G as the parameter controlling the strength of the gain in the different regions of space. This choice automatically includes the possibility of having different atomic densities in the different regions; compared to the pumping rate γ_g, it also allows us to simplify the presentation by avoiding the complications due to the simultaneous dependence of several other parameters on γ_g.

The numerical results that are presented in Secs. III and IV were obtained by numerically simulating the system evolution described by Eq. (4) via a standard fourth order Runge–Kutta integration scheme that provides direct access to time-dependent quantities. The steady-state values of observable are extracted by running the time-dependent simulations up to very long times. The lasing frequency and the power spectral density are obtained by Fourier transform of the late-time temporal evolution of the relevant field amplitudes.

B. Frequency-dependent gain

The peculiar features of the frequency-dependent gain can be simply understood by looking at the laser operation in a single site geometry. Indicating with ω_L the lasing frequency, the steady-state is determined by the late-time behavior of the solution to the Bloch equations (4) in the single-site case.

In this limit, the atomic populations tend to have a constant value, while both the coherence ρ_{eg} and the field amplitude α keep oscillating at frequency ω_L. The explicit expressions for the steady-state atomic quantities are given in the supplementary material. The steady-state field amplitude is instead $\alpha(t) = \tilde{\alpha}\, e^{-i\omega_L t}$ with the amplitude $\tilde{\alpha}$ satisfying the gain/loss balance equation

$$\frac{P}{1+\beta|\tilde{\alpha}|^2} = \Gamma, \tag{5}$$

with the effective pump strength

$$P = G\left(\frac{\gamma}{(\omega_{eg}-\omega_L)^2+\gamma^2}\right)\left(\frac{\gamma_g-\gamma_e}{\gamma_g+\gamma_e}\right) \tag{6}$$

and the saturation coefficient

$$\beta = 2\frac{g^2}{\gamma_{eg}}\left(\frac{\gamma}{(\omega_{eg}-\omega_L)^2+\gamma^2}\right). \tag{7}$$

Equation (5) is formally analogous to the one of a broadband saturable gain considered in Refs. 5 and 23, with the key difference that the parameters P, β are here frequency-dependent. In particular, the effective pump strength P involves a Lorentzian factor $\gamma/[(\omega_{eg}-\omega_L)^2+\gamma^2]$ accounting for the non-trivial gain spectrum: this is centered at ω_{eg} and has a HWHM set by the atomic decoherence rate γ.

This frequency-dependent gain directly reflects into an analogous dependence of the laser threshold. In a single-site geometry, this is immediately obtained from Eqs. (5) and (6) as the lowest value of G for which (unsaturated) gain exceeds losses $P \geq \Gamma$. This leads to the threshold condition

$$G > G_{\mathrm{res},0}\left[1+\left(\frac{\omega_L-\omega_{eg}}{\gamma}\right)^2\right], \tag{8}$$

where

$$G_{\mathrm{res},0} \doteqdot \frac{2\gamma_{eg}\gamma\Gamma}{\gamma_g-\gamma_e} \tag{9}$$

is the single-cavity lasing threshold exactly on resonance, that is, for $\omega_L = \omega_{eg}$. As expected, the threshold is minimum when laser operation occurs on resonance with the population-inverted atoms. Then, it increases quadratically with the detuning $\omega_L - \omega_{eg}$: the faster the atomic decoherence rate γ, the weaker this increase. In the following, we will exploit this frequency dependence of the threshold as a way to select the desired mode for lasing.

III. NARROWBAND GAIN

In Sec. II B, we have restricted our attention to the single-site case. This provides us the conceptual building blocks to understand laser operation in a topological lattice. As a first step in this direction, in this section, we consider the simplest case where the narrowband gain spectrum is concentrated within a topological gap. In contrast to the chaotic multi-mode emission found in Ref. 23 for the extreme broadband gain, here we show that such narrowband gain can lead to a stable topological lasing even under a spatially uniform pumping. While such a narrowband gain might not be the technologically simplest option for practical devices, a detailed discussion of its features is an interesting first step to validate our Bloch–Harper–Hofstadter model and understand its behavior in the different regimes. In addition to that, because of mode-pulling effects, an interesting nontrivial relation is found between the lasing frequency and the bare frequencies of the discrete set of edge modes.

A. Single-mode topological laser emission

This narrowband gain configuration can be obtained by considering the Bloch–Harper–Hofstadter model introduced in Sec. II A and tuning the atomic frequency ω_{eg} in the middle of the topological bandgap with a gain linewidth γ much smaller than the gap width, as sketched in Fig. 2(c). In this way, the frequency dependence of gain strongly increases the effective threshold for laser operation in the off-resonant bulk band states, while the one for edge state lasing remains almost unaffected.

Laser operation in this regime is illustrated in Figs. 2(a) and 2(b). Emission into the edge state is stable and monochromatic and remains so up to high pump strengths well above the laser threshold.[34] Quite interestingly, such monochromatic single-mode emission is not restricted to small lattice sizes where a single eigenstate—classified by k_y for the strip geometry of Fig. 2(c) or by the winding number around the lattice for the geometry of Fig. 2(a)—falls within the gain bandwidth: as it was pointed out in Ref. 23 for the extreme broadband gain case, the high spatial overlap

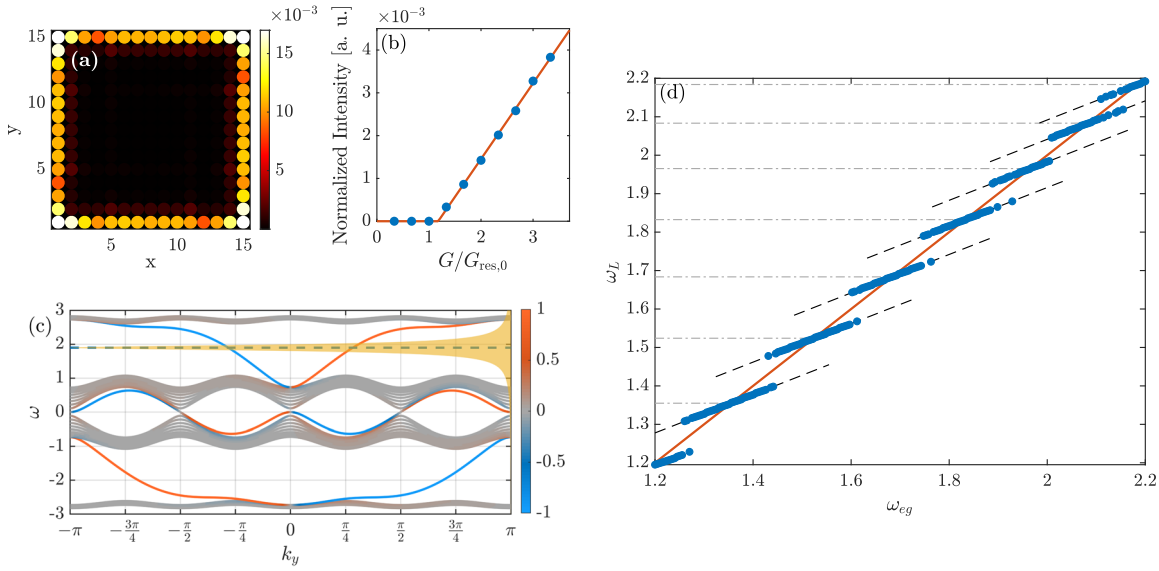

FIG. 2. (a) Steady state emission of a 15 × 15 lattice, uniformly pumped on all sites with a narrowband gain of strength $G/G_{\mathrm{res},0} = 3$. The atomic transition frequency is $\omega_{eg} = 1.9$. For these parameters, lasing is found to occur at $\omega = 1.87$. (b) Spatially averaged emitted intensity as a function of the gain strength G, showing the typical linear behavior after the lasing threshold. (c) Band structure of a Harper–Hofstadter lattice with PBCs in the y-direction but finite in the x-direction $N_x = 39$. The color scale from blue to red quantifies the localization of each mode from left to right in the x-direction, while the dashed line indicates the atomic resonance ω_{eg}. The narrowband gain used for the simulations in the panels above is represented as a Lorentzian in the frequency domain, centered at ω_{eg} and with a FWHM of $2\gamma = 0.2$, i.e., roughly 13% of the topological bandgap. (d) Numerically observed lasing frequency (blue dots) as a function of the atomic resonance frequency ω_{eg}. Each slant step is fitted with a black dashed line with equation $\omega_L = \frac{1}{2}\omega_{eg} + b$. The light gray dashed-dotted lines mark the lasing frequency values for which $\omega_L = \omega_{eg} = \omega_0$ [see (10)], while the red line represents the approximated curve $\omega_L = \omega_{eg}$. The simulations have been performed by numerically integrating the Bloch–Harper–Hofstadter motion equations (4) up to a time $T = 500\ \Gamma^{-1}$; the other parameters are the same as in the left panels. All frequencies are measured in units of the hopping J and the zero is at the bare cavity frequency ω_{cav}. The lasing frequency is extracted from the power spectral density of the emission that is obtained by a temporal Fourier transform of the light field amplitude in the latest $\Delta T = 150\ \Gamma^{-1}$ of the evolution.

of different edge states provides, in fact, a very efficient mode competition mechanism[32] eventually suppressing simultaneous laser operation in multiple modes. The dynamical stability of the single mode emission was confirmed by the Bogoliubov analysis in Ref. 35. A further illustration of the dynamics of this mode-competition process over time is provided in Sec. S.3 of the supplementary material where we display a time-frequency representation of the lasing process. As usual, the choice of the specific lasing mode is stochastically determined at each instance of lasing by the initial conditions and the noise. Still, for sufficiently narrowband gain, the resulting probability distribution for lasing in different modes will be very peaked on the most likely mode.

Of course, this monochromatic emission only holds up to moderate pump strengths at which only the quasi-resonant edge modes experience an effective gain. At very high pump strength, also the bulk modes go above threshold and the dynamics recovers the chaotic behavior found in Ref. 23 for a broadband gain distributed in the whole system.

B. Mode-pulling effects

In contrast to the broadband gain case where the laser frequency ω_L is typically locked to the bare mode frequency ω_0, for a narrowband gain, a sizable *mode-pulling* effect can occur on the laser frequency.[33] The lasing frequency results then from a weighted average of the atomic resonance ω_{eg} and the bare mode frequency ω_0 via the mode pulling formula

$$\omega_L = \frac{\omega_0 + \mathcal{S}\omega_{eg}}{1 + \mathcal{S}}, \tag{10}$$

where $\mathcal{S} = \Gamma/\gamma$ is the so-called the *stabilization factor*. When $\mathcal{S} \ll 1$ mode-pulling effects are negligible and $\omega_L = \omega_0$, where ω_0 is the frequency of the corresponding lattice mode selected by the lasing process. For equal $\Gamma = \gamma$, the stabilization factor is $\mathcal{S} = 1$ and the mode-pulling effect becomes a simple average. Physically, this mode-pulling effect can be understood as a result of the refractive index change that is naturally associated with the gain via Kramers–Kronig causality relations: as usual, narrow resonances are responsible for quantitatively larger changes of the refractive index in their spectral neighborhood.

Let us explore the impact of this effect in our case of topological laser operation for a narrowband gain centered inside the topological bandgap, thus perfectly overlapping with the edge state dispersion. The blue dots in Fig. 2(d) show the numerical prediction for the steady-state lasing frequency as a function of the atomic resonance position ω_{eg}. This plot illustrates an interesting interplay of mode pulling with the intrinsic discreteness of the edge state.[23] Given the finite size of the system, the edge state consists, in fact, of a sequence of discrete states classified by the winding number around

the perimeter of our square sample. In Fig. 2(d), the frequencies of such states are indicated by the horizontal dashed-dotted lines.

When mode-pulling effects are negligible, for instance, in a broadband gain case, the system lases at the frequency of the edge mode that is closest to the resonance ω_{eg} for which gain is the strongest. In our plot, this would correspond to a staircase of flat steps separated by a spacing $\Delta\omega = 2\pi v_g/L$ determined by the overall length L of the system edge and the group velocity v_g of the edge mode.

For our narrowband gain, laser operation still occurs in the discrete mode that is closest to ω_{eg}, but mode-pulling effects make the steps to have a finite slope instead of being flat. Inserting the frequency of the selected edge state as the cavity frequency ω_0 in (10) predicts a value $\frac{\mathcal{S}}{1+\mathcal{S}}$ for the slope. In the figure, we have taken $\gamma = \Gamma$, so the stabilization factor is $\mathcal{S} = 1$ and the expected slope is $1/2$. This value (black dashed lines) is in perfect agreement with the numerical findings.

IV. BROADBAND GAIN

In Sec. III, we have seen an efficient scheme to stabilize topolaser operation with a uniformly distributed gain by spectrally concentrating the gain spectrum in the topological gap. While conceptually interesting, this scheme is hardly useful in practical semiconductor systems, where the gain linewidth is typically comparable if not larger than the width of the topological bandgaps so that an efficient spectral selection of the edge mode from the neighboring bulk modes is hardly obtained.

In this section, we will explore a more sophisticated scheme that is able to stabilize topological lasing in a much wider range of parameters of potential technological relevance. The configuration we consider is inspired by the photonic crystal experiment in Ref. 17 where the topological bandgap is orders of magnitude narrower that the gain linewidth. One of the aims of our work is to provide theoretical insight into the observed single-mode topolaser emission of this experiment.

A sketch of the configuration under examination is shown in Fig. 3(d). As in the experiment,[17] we consider a central region, which has a narrow topological gap, surrounded by a region with a much wider and topologically trivial gap. Chiral boundary modes are localized at the interface between the two regions. We also assume that the gain bandwidth is much larger than the narrow topological gap but comparable to the large trivial gap, as in the experiment, and that the gain is stronger in the trivial region than in the topological region. As a consequence, even though the gain material is pumped in a globally spatially uniform fashion, we can expect clear topolaser operation in the edge states that partially penetrate into the trivial region with stronger gain, while lasing into the bulk states of the trivial region is suppressed by their detuning from the gain bandwidth. In this section, we explain in detail how this idea works.

We first explain how we model a narrow and isolated topological gap in the central region. We start from the $\vartheta = 1/4$ Harper–Hofstadter lattice, which contains multiple topological bandgaps with topological invariants adding up to zero. We want to isolate one topological bandgap from these multiple gaps. To this end, we add a checkerboard-shaped on-site frequency detuning $\pm\Delta$: the frequencies of the (m, n) sites are thus alternated and equal to $\omega_{\text{cav}} + \Delta \cdot (-1)^{m+n}$. The photonic bands of such a *bipartite* Harper–Hofstadter model are shown in panel (a) of Fig. 3: because of the checkerboard detuning, the Brillouin zone is reduced to $k_y \in \left[-\frac{\pi}{2}, \frac{\pi}{2}\right]$ and the Dirac touching points between the middle two bands open into a trivial gap with size $\sim 2\Delta$. In agreement with the sequence $-1, +1, +1, -1$ of Chern numbers of the different bands, the two (small) gaps between the lower two bands and the upper two bands maintain their topological nature visible in the corresponding edge states. In what follows, we focus on the topological bandgap of the two upper bands; the gain spectrum is centered around the frequency of the two upper bands. The two lower bands are, instead, off-resonant and are not relevant in the laser operation and the discussion below.

Next, we explain how we prepare the surrounding region with a wide trivial gap. We again start from the $\vartheta = 1/4$ Harper–Hofstadter model and add a checkerboard-shaped detuning Δ_{trivial}, which is larger than $\pm\Delta$ in the topological region. We add a global shift of all site frequencies by ω_{trivial} so that the large topologically trivial gap between the middle two bands is centered around the two upper bands of the topological region. The corresponding photonic bands are shown in panel (b). Although the two upper and two lower bands have narrow topological gaps, they are pushed away by the large Δ_{trivial}, and thus, we can focus on the effect of the wide trivial gap between the middle two bands. We call this surrounding region a "trivial" region in this sense. The gain spectrum, which is indicated by the yellow shading in panels (a) and (b), is centered at the middle of the wide trivial gap and completely encompasses the topological gap in the central region.

The gain strength in the surrounding trivial region, G_{trivial}, can be reinforced either by locally increasing the pumping strength or, alternatively, by keeping a spatially uniform pumping but increasing the density of the gain material with respect to the central region, as discussed in Sec. II A. Focusing on the latter case, which appears relevant for the experiment in Ref. 17, we can write $G_{\text{trivial}} = G \cdot d$, where d can be interpreted as the effective density of the gain material in the surrounding region relative to the central region, and treat $G/G_{\text{res},0}$ as a global measure of the uniformly distributed pumping strength in units of the single-resonator resonant threshold.

The results of the numerical simulations are summarized in Fig. 3, where we show a phase diagram of the different regimes of laser operation as a function of the relative effective density of the gain material in the surrounding region $d = G_{\text{trivial}}/G$ and of the pumping strength in the central topological region in units of the resonant, single-site threshold, $G/G_{\text{res},0}$.

When the surrounding trivial region is purely passive and does not display any gain [$d = 0$, Figs. 3(i) and 3(j)], the system is almost equivalent to a bipartite 15×15 lattice without the surrounding region. We, therefore, expect the system to only lase above the resonant single-site lasing threshold, $G/G_{\text{res},0} = 1$, as shown by the red region at the bottom of the phase diagram. Since the gain is effectively broadband with respect to the upper pair of photonic bands in the central region, both bulk and boundary modes equally participate in the lasing process, forbidding a stable topological laser operation [panel (j)]. Compared to the bulk states, boundary states are even slightly disfavored by the worse spectral overlap with the gain spectrum and by their evanescent tail that penetrates into the surrounding trivial region and reduces the spatial overlap with the gain region.

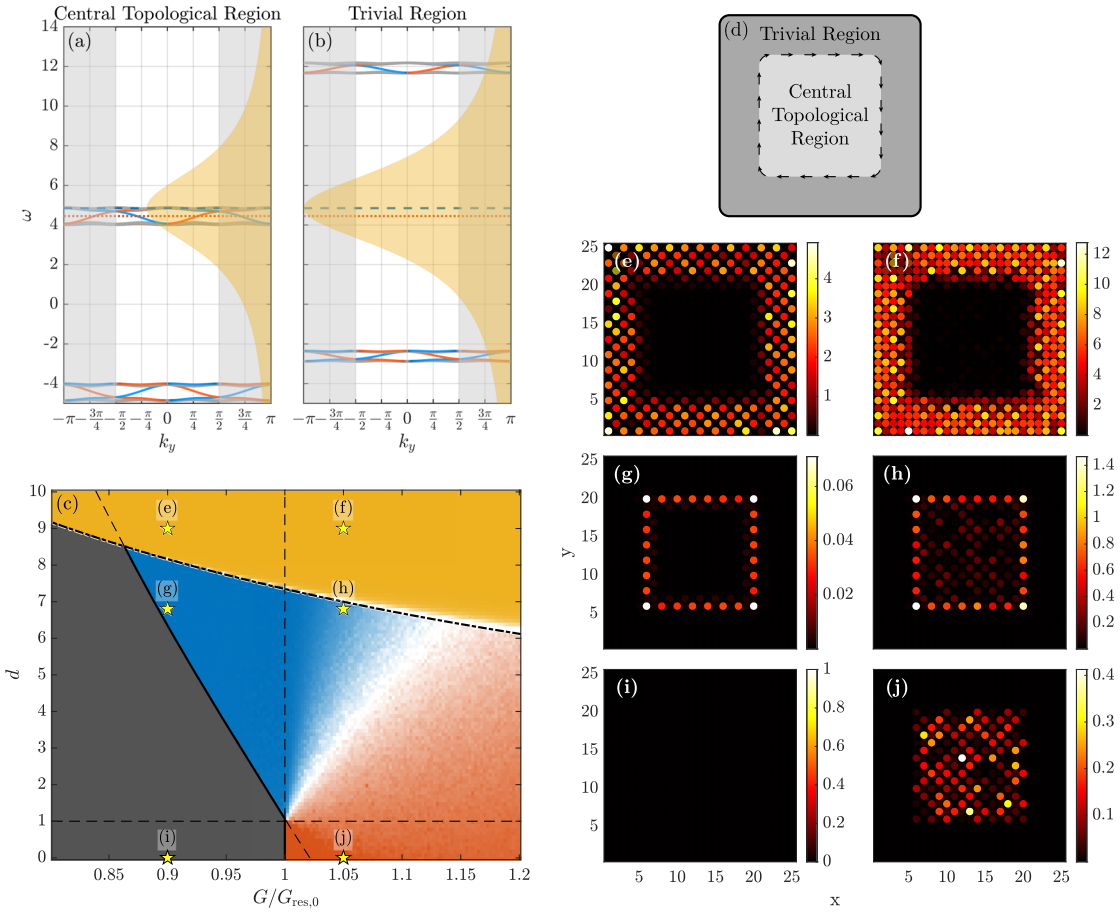

FIG. 3. Result of simulations performed on a 25 × 25 lattice with a five-site thick surrounding region. (a) and (b) Band structure for the proposed broadband scheme, with a geometry schematically depicted in panel (d). The central region [panel (a)] is a bipartite $\vartheta = 1/4$ Harper–Hofstadter lattice with checkerboard detuning $\Delta = 4.0$, while the surrounding region [panel (b)] has the same geometry with a larger checkerboard detuning $\Delta_{\mathrm{trivial}} = 7.0$ and a global detuning $\omega_{\mathrm{trivial}} = 4.65$ (red dotted line). The gain spectrum is centered at $\omega_{eg} = 4.85$ (blue dashed line) and has a FWHM linewidth $2\gamma = 5.2$ (yellow shading). The relative strength of gain on the two sides depends on $d = G_{\mathrm{trivial}}/G$: for the specific case illustrated in the figure, the taller gain spectrum in panel (b) refers to a $d > 1$ case of stronger gain in the trivial region. The gray shaded areas indicate k_y-vectors outside the reduced Brillouin zone. For these parameters, the gain linewidth is around 8.2 times larger than the width of the topological bandgap of the central region and around 37% of the width of the trivial bandgap in the surrounding region. It is around 63 times wider than the one considered in Fig. 2. (c) Phase diagram of the different lasing regimes as a function of the overall pumping strength $G/G_{\mathrm{res},0}$ and of the relative effective density of the gain material of the surrounding region $d = G_{\mathrm{trivial}}/G$ for the same lattice parameters used in the dispersion plots shown in the top left panels. The gray color indicates no lasing; the blue color indicates lasing from the topological edge mode; the red color indicates lasing from the non-topological portion of the central region; and the yellow color indicates lasing from the surrounding region. Fading to white indicates the coexistence of multiple phases. The thin dashed black lines indicate the $G/G_{\mathrm{res},0} = 1$ and $d = 1$ values. The solid and dotted-dashed black transition lines between different phases are analytically predicted via the prescriptions in Sec. S.5 of the supplementary material. The six yellow stars have a one-to-one correspondence with panels (e)–(j) presented on the right, showing sample snapshots of the real-space emitted intensity at the end of the integration time. The first, second, and third rows from the top are for decreasing values of $d = 9.0, 6.8$, and 0, respectively. The left and right columns are for increasing $G/G_{\mathrm{res},0} = 0.90$ and 1.05, respectively, below and above the single-site resonant lasing threshold. All simulations have been performed by numerically integrating the Bloch–Harper–Hofstadter motion equations (4) up to a time $T = 10^4\Gamma^{-1}$.

We can induce lasing from the topological edge modes at the boundary by making the gain in the surrounding trivial region to be stronger than the one in the central topological region, that is, $d > 1$. In this case, a region appears in the parameter space where the system displays a monochromatic topological laser behavior [panel (g)]. Thanks to their evanescent tail overlapping with the stronger amplifying surrounding region, the effective threshold of the topological boundary modes is, in fact, pushed well below the one $G/G_{\mathrm{res},0} = 1$ of the bulk modes (thick solid black line in the phase diagram), opening a window where only these modes can lase (blue region). In this $G/G_{\mathrm{res},0} < 1$ regime, the monochromaticity of the topolaser emission is ensured by the same mode competition effects pointed out in Ref. 23 and reviewed in Sec. III: since only topological edge modes experience a sufficient gain to lase and since these modes spatially share the same active medium, steady-state lasing ends up being concentrated in one of them only, thus making the emission

monochromatic. A more detailed time-frequency analysis in support of this conclusion is reported in Sec. S.3 of the supplementary material.

In order to better quantify the efficiency of our combined mode-selection scheme, we have investigated the constraints on the gain linewidth γ in order to have pure topolaser operation into the edge state. Quite interestingly, topolasing turns out to be robust as long as the effective gain experienced by the bulk bands in the trivial region remains below threshold. As it can be inferred from the discussion in Sec. S.5 of the supplementary material, for sufficiently large Δ_{trivial}, the upper bound on γ involves only $\gamma/\Delta_{\text{trivial}}$. In particular, no restriction applies to the ratio of γ to the topological gap width. In the experiment of Ref. 17, the analog of Δ_{trivial} is way larger than the topological bandgap, which releases any constraint on the gain bandwidth compared to the topological gap and allows the latter to be arbitrarily small.

Note that this spectral structure is characteristic of the photonic crystal platform of Ref. 17 and is different from the typical one of the ring-resonator-based platforms considered in Ref. 18. Here, additional copies of the band structure are, in fact, present with a spacing set by the (relatively small) free spectral range of the single ring resonators and our mode-selection mechanism is not applicable in a straightforward way.

The situation is of course very different in the $G/G_{\text{res},0} > 1$ case, when also the bulk modes of the topological region go above threshold. Since these modes have a reduced spatial overlap among them and with the edge mode, mode competition is no longer effective in ensuring a monochromatic emission and the latter acquires a complex multi-mode character (blue-to-white-to-red region). Still, thanks to the stronger gain of the surrounding trivial region, the intensity of boundary mode lasing can remain significantly stronger than the one of the central bulk modes even at values of G above the single-cavity lasing threshold [panel (h)].

For even higher values of the surrounding density d above the dashed-dotted black line in the phase diagram, we reach a point where the spectral selection is no longer sufficient to suppress bulk lasing in the surrounding region and topological lasing is no longer possible. In this phase (yellow area in the phase diagram), the much stronger gain of the surrounding region makes the laser emission to be concentrated in this region [panels (e) and (f)].

A quantitative analytical discussion of the location of the transition lines in the phase diagram is given in Sec. S.5 of the supplementary material. As expected, the area of the topological lasing region in parameter space can be increased by either increasing the trivial bandgap in the surrounding region or using a narrower gain spectrum. This trend is confirmed by the additional numerical simulations with different values of the parameters that are shown in Sec. S.4 of the supplementary material.

V. DISCUSSION

In Secs. II–IV, we have concentrated our attention on a Harper–Hofstadter model that provides a relatively straightforward insight into the basic effects, but our conclusions extend to any combination of lattices with suitable spectral and topological properties. In particular, we expect that our physical conclusions extend even outside the tight-binding approximation that has been made in all theoretical studies of topological lasing so far.

As a most intriguing example, the results of our calculations are compatible with some key observations of the pioneering experiment in Ref. 17 that, to the best of our knowledge, remain so far unexplained. In particular, topological lasing was observed in this experiment without the need to concentrate gain along the edge separating the topological and trivial regions as it was instead the case in other experiments.[18,19] A key difference between the devices used in these works consists in that the topological system used in Ref. 18 is surrounded by empty space, while in Ref. 17 the central topological system is surrounded by a topologically trivial region where the field can penetrate with a significant evanescent tail. Most importantly for our purposes, the outer region displays a larger filling factor of the unit cell (compare Figs. 2A and 2B in Ref. 17). For an equal level of optical pumping, we can thus reasonably expect the gain to be stronger in the outer region, which corresponds to $d > 1$ in our model. As a result, the overlap of the edge state with this stronger amplifying region favors topological lasing with respect to bulk lasing in the central region. At the same time, the much wider extension of the trivial photonic bandgap of the outer region forbids laser operation in the outer region thanks to the natural frequency dependence of gain in the used semiconductor quantum well material.

While these arguments provide a suggestive interpretation of experimental observations, they are of course not yet completely sufficient to rule out other possible explanations. For instance, in analogy to the arguments put forward in Ref. 20 for a different geometry, another potentially relevant mechanism for stabilizing the edge mode lasing could originate from the weaker losses of the edge mode compared to the ones of bulk modes.[36] In the specific system of Ref. 17, reduced radiative losses may, in fact, originate from the evanescent tail in the outer trivial region where bulk modes in the vicinity of the trivial gap are below the light cone. In our model theory, the reduced radiative losses of the trivial region could be explicitly included via a reduced Γ of the outer sites, but we expect their effect to be similar to the one of the increased gain G_{trivial} considered in our calculations. On this basis, we are confident that the qualitative conclusions of our theory directly apply to the experiment. However, a firm and definitive unraveling of these questions requires accurate experimental measurements and comprehensive microscopic calculations of the band structure and of the radiative and non-radiative decay rates of the different modes,[36] which go beyond our work.

As a final point, it is worth briefly mentioning some straightforward experiments that may serve to shed light on the possible interpretations of the experimental observations even in the absence of a direct measurement of the Q factor of the different modes. In the IR spectral region of the experiment, magnetic effects are quite weak as signaled by the smallness of the topological gap. This implies that the magnetic field is crucial to induce the topological edge state but has a minor effect on the bulk regions. As a result, according to our theory in the absence of any magnetic field, no laser operation should be observed up to powers well above the topological laser threshold. Some evidence in this direction is found by comparing Figs. 3(b) and 3(c) of Ref. 17. Further experimental insight could be obtained by keeping the magnetic field on and ramping up the pump intensity well above the topological laser threshold. According to our model, as discussed in Sec. IV, going up in gain strength G should move the system from the topological lasing region indicated in blue into the ones of multimode bulk lasing indicated in red/yellow. In

particular, we expect that the threshold for bulk lasing at high gain strengths should be almost insensitive to the applied magnetic field.

VI. CONCLUSIONS

In this work, we have developed a general semiclassical theory of topological laser operation that is able to include the peculiar structure of the photonic modes of the underlying topological lattice and the frequency dependence of a realistic gain material. As a specific example of application of our theory, we have investigated the lasing threshold in a configuration that displays a subtle interplay between the spatial overlap of the modes with the gain medium and the spectral position and width of the frequency gaps in the different regions. Based on our theory, we propose an interpretation of the recent experiments in Ref. 17, where stable topolaser emission was observed despite the gain being distributed across the whole photonic crystal structure and not localized on the topological edge as in Ref. 18.

A natural next step will be to include our theory of frequency-dependent gain into the Bogoliubov description of collective excitations around a topologically lasing state[35] so as to characterize the stability of realistic models of topological laser operation in the different regimes of gain parameters. This will be of great interest as a new tool to tame all those instability mechanisms that may hinder a clean and efficient single-mode topological laser emission in practical semiconductor devices.

SUPPLEMENTARY MATERIAL

See the supplementary material for full derivations of the theoretical models, additional simulations at different gain widths, and an extended discussion on the topological lasing features.

ACKNOWLEDGMENTS

We warmly acknowledge continuous stimulating exchanges with Boubacar Kanté. We are grateful to Aurelian Loirette-Pelous and Ivan Amelio for continuous discussions on topolaser dynamics, and we thank Maxim Gorlach for discussions on our preliminary results. We acknowledge financial support from the European Union H2020-FETFLAG-2018-2020 project "PhoQuS" (Grant No. 820392) and from the Provincia Autonoma di Trento. T.O. acknowledges support from JSPS KAKENHI Grant No. JP20H01845, JST PRESTO Grant No. JPMJPR19L2, and JST CREST Grant No. JPMJCR19T1. The numerical simulations were performed on SISSA's Ulysses cluster.

DATA AVAILABILITY

The data that support the findings of this study are available from the corresponding author upon reasonable request.

REFERENCES

[1] T. Ozawa, H. M. Price, A. Amo, N. Goldman, M. Hafezi, L. Lu, M. C. Rechtsman, D. Schuster, J. Simon, O. Zilberberg, and I. Carusotto, Rev. Mod. Phys. **91**, 015006 (2019).
[2] Y. Ota, K. Takata, T. Ozawa, A. Amo, Z. Jia, B. Kante, M. Notomi, Y. Arakawa, and S. Iwamoto, Nanophotonics **9**, 547 (2020).
[3] G. Harari, M. A. Bandres, Y. Lumer, Y. Plotnik, D. N. Christodoulides, and M. Segev, in *Conference on Lasers and Electro-Optics* (OSA, Washington, DC, 2016), p. FM3A.3.
[4] S. Wittek, G. Harari, M. A. Bandres, H. Hodaei, M. Parto, P. Aleahmad, M. C. Rechtsman, Y. Chong, D. Christodoulides, M. Khajavikhan, and M. Segev, in *Conference on Lasers and Electro-Optics* (Optical Society of America, Washington, DC, 2017), p. FTh1D.3.
[5] G. Harari, M. A. Bandres, Y. Lumer, M. C. Rechtsman, Y. D. Chong, M. Khajavikhan, D. N. Christodoulides, and M. Segev, Science **359**, eaar4003 (2018).
[6] L. Pilozzi and C. Conti, Phys. Rev. B **93**, 195317 (2016).
[7] D. D. Solnyshkov, A. V. Nalitov, and G. Malpuech, Phys. Rev. Lett. **116**, 046402 (2016).
[8] P. St-Jean, V. Goblot, E. Galopin, A. Lemaître, T. Ozawa, L. Le Gratiet, I. Sagnes, J. Bloch, and A. Amo, Nat. Photonics **11**, 651 (2017).
[9] M. Parto, S. Wittek, H. Hodaei, G. Harari, M. A. Bandres, J. Ren, M. C. Rechtsman, M. Segev, D. N. Christodoulides, and M. Khajavikhan, Phys. Rev. Lett. **120**, 113901 (2018).
[10] C. Han, M. Lee, S. Callard, C. Seassal, and H. Jeon, Light: Sci. Appl. **8**, 40 (2019).
[11] Y. Ota, R. Katsumi, K. Watanabe, S. Iwamoto, and Y. Arakawa, Commun. Phys. **1**, 86 (2018).
[12] H. Zhao, P. Miao, M. H. Teimourpour, S. Malzard, R. El-Ganainy, H. Schomerus, and L. Feng, Nat. Commun. **9**, 981 (2018).
[13] W. Zhang, X. Xie, H. Hao, J. Dang, S. Xiao, S. Shi, H. Ni, Z. Niu, C. Wang, K. Jin, X. Zhang, and X. Xu, Light: Sci. Appl. **9**, 109 (2020).
[14] H.-R. Kim, M.-S. Hwang, D. Smirnova, K.-Y. Jeong, Y. Kivshar, and H.-G. Park, Nat. Commun. **11**, 5758 (2020).
[15] Y. V. Kartashov and D. V. Skryabin, Phys. Rev. Lett. **122**, 083902 (2019).
[16] I. Amelio and I. Carusotto, Phys. Rev. X **10**, 041060 (2020).
[17] B. Bahari, A. Ndao, F. Vallini, A. El Amili, Y. Fainman, and B. Kanté, Science **358**, 636 (2017).
[18] M. A. Bandres, S. Wittek, G. Harari, M. Parto, J. Ren, M. Segev, D. N. Christodoulides, and M. Khajavikhan, Science **359**, eaar4005 (2018).
[19] Y. Zeng, U. Chattopadhyay, B. Zhu, B. Qiang, J. Li, Y. Jin, L. Li, A. G. Davies, E. H. Linfield, B. Zhang, Y. Chong, Q. J. Wang *et al.*, Nature **578**, 246 (2020).
[20] W. Noh, H. Nasari, H.-M. Kim, Q. Le-Van, Z. Jia, C.-H. Huang, and B. Kanté, Opt. Lett. **45**, 4108 (2020).
[21] S. Longhi, Y. Kominis, and V. Kovanis, Europhys. Lett. **122**, 14004 (2018).
[22] S. Malzard and H. Schomerus, New J. Phys. **20**, 063044 (2018).
[23] M. Seclì, M. Capone, and I. Carusotto, Phys. Rev. Res. **1**, 033148 (2019).
[24] M. Seclì, "Edge state lasing in a 2D topological photonic system," M.Sc. thesis, University of Trento, Trento, 2017.
[25] Y. Gong, S. Wong, A. J. Bennett, D. L. Huffaker, and S. S. Oh, ACS Photonics **7**, 2089 (2020).
[26] H. Zhong, Y. Li, D. Song, Y. V. Kartashov, Y. Zhang, Y. Zhang, and Z. Chen, Laser Photonics Rev. **14**, 2000001 (2020).
[27] H. E. Türeci, A. D. Stone, and B. Collier, Phys. Rev. A **74**, 043822 (2006).
[28] E. J. Bergholtz, J. C. Budich, and F. K. Kunst, Rev. Mod. Phys. **93**, 015005 (2021).
[29] K. Kawabata, K. Shiozaki, M. Ueda, and M. Sato, Phys. Rev. X **9**, 041015 (2019).
[30] M. Hafezi, S. Mittal, J. Fan, A. Migdall, and J. M. Taylor, Nat. Photonics **7**, 1001 (2013).
[31] D. R. Hofstadter, Phys. Rev. B **14**, 2239 (1976).
[32] M. Sargent, M. O. Scully, and W. E. Lamb, *Laser Physics*, 1st ed. (Westview Press, 1974).
[33] M. O. Scully and M. S. Zubairy, *Quantum Optics* (Cambridge University Press, 1997).
[34] M. Seclì and I. Carusotto, in *2019 Conference on Lasers and Electro-Optics Europe and European Quantum Electronics Conference* (IEEE, 2019), p. 1.
[35] A. Loirette-Pelous, I. Amelio, M. Seclì, and I. Carusotto, arXiv:2101.11737 (2021).
[36] B. Bahari, L. Hsu, S. H. Pan, D. Preece, A. Ndao, A. El Amili, Y. Fainman, and B. Kanté, Nat. Phys. **4**, 4–8 (2021).